Journal of Materials Chemistry A

ROYAL SOCIETY OF CHEMISTRY

PAPER

View Article Online
View Journal | View Issue

Cite this: J. Mater. Chem. A, 2022, 10, 24156

Modulating between 2e⁻ and 4e⁻ pathways in the oxygen reduction reaction with laser-synthesized iron oxide-grafted nitrogen-doped carbon†

Huize Wang, ‡[a] Maria Jerigova,‡[a] Jing Hou, [a] Nadezda V. Tarakina, [a] Simon Delacroix, [b] Nieves López-Salas *[a] and Volker Strauss *[a]

In this study, we demonstrate the tuning of the oxygen reduction reaction (ORR) using iron/iron oxide nanoparticle grafted laser-patterned nitrogen-doped carbon (LP-NC) electrodes. Depending on the preparation route, *i.e.* addition of a molecular $Fe(NO_3)_2$ precursor before (route 1) or after pre-carbonization (route 2) of the citric acid/urea precursors, either the 4e⁻ or the 2e⁻ pathway in the ORR is facilitated leading to either H_2O or H_2O_2 as a reaction product, respectively. The kinetic reaction conditions afford mixed valence metal oxide nanoparticles embedded in LP-NC in the form of either Fe_2O_3/Fe or Fe_2O_3/FeO/Fe, respectively, facilitated by an *in situ* carbothermal reduction during the laser-induced carbonization. In HR(S)TEM analysis we found evidence for the occurrence of Fe_2O_3 in the η- or α-phase, depending on the preparation route. Reciprocally, the graphitization is also affected by the preparation route leading to either homogeneous graphitization or a locally graphitized shell structures around the nanoparticles. In the 4e⁻ mediated ORR facilitated by η-Fe_2O_3/Fe@LP-NC onset potentials as low as 0.70 V (*vs.* RHE) with a H_2O_2 production efficiency of 4% and 10% in alkaline and neutral electrolyte, respectively, were determined. On the other hand, α-Fe_2O_3/FeO/Fe@LP-NC presents an onset potential for the 2e⁻ mediated ORR as low as 0.77 V with a H_2O_2 production efficiency of nearly 80%. The changes in selectivity and physicochemical properties of the electrocatalysts by applying simple modifications in the synthetic route point to laser-patterning as a very promising route to scale up designer electrodes for electrochemical conversion.

Received 24th July 2022
Accepted 2nd October 2022

DOI: 10.1039/d2ta05838c

rsc.li/materials-a

Introduction

In the face of current global energy and environmental challenges, the development of alternative energy conversion systems has become increasingly critical. In this regard, electrochemical energy conversion facilitated by sustainable electrocatalysts is expected to be a frontrunner in future energy supply.[1] An essential reaction in a number of electrocatalytic applications is the oxygen reduction reaction (ORR), in which molecular oxygen (O_2) is electrochemically reduced to either H_2O or H_2O_2 following the 4e⁻ or 2e⁻ pathway, respectively.[2] In the ORR process, the common intermediate adsorbate on the catalyst interface is *–OOH (* denotes an active site). Depending on the active sites and the catalyst design either the dissociation at the active site (*–OOH) or the O–O bond (*O–OH) is favoured, resulting in the formation of H_2O_2 or $2H_2O$, respectively. According to the standard potentials the 4e⁻ pathway is thermodynamically preferred.[3]

The latter is applied in state-of-the-art proton-exchange membrane (PEM) fuel cells to convert chemical energy into electric energy.[4] Today, carbon-supported platinum (Pt) is the preferred choice of a catalyst system in commercial devices to achieve the best economic ORR performance.[5] Such systems provide excellent reaction kinetics and flexibility.[6,7] However, high costs due to limited natural reserves and rapid deactivation due to the inevitable phenomenon of methanol crossover are still limiting factors for the widespread practical application of PEM fuel cells.[8] Furthermore, the 4e⁻ ORR is used in metal-air batteries.[9] On the other hand, H_2O_2 formed in the 2e⁻ reduction pathway is a valuable chemical used in many applications such as paper production, chemical synthesis, or water treatment,[10] and is currently produced by a highly energy-consuming process of anthraquinone oxidation.[11] However, the production of cheap and stable catalysts showing high selectivity towards the 2e⁻ reduction pathway is still a topic of research.[12]

[a]Department of Colloid Chemistry, Max Planck Institute of Colloids and Interfaces, Am Mühlenberg 1, 14476 Potsdam, Germany. E-mail: Nieves.LopezSalas@mpikg.mpg.de; volker.strauss@mpikg.mpg.de

[b]LPICM, CNRS UMR 7647, Ecole polytechnique, Institut Polytechnique de Paris, Palaiseau 91128, France

† Electronic supplementary information (ESI) available. See https://doi.org/10.1039/d2ta05838c

‡ Contributed equally.

To avoid the use of expensive noble metals, abundant transition metals on carbon supports with competitive catalytic activity and selectivity for the ORR are a promising alternative.[13] For instance, iron oxides (α-Fe_2O_3,[14] γ-Fe_2O_3 (ref. 15 or Fe_3O_4 (ref. 16) or iron carbides[17,18] have been shown to catalyze the $4e^-$ pathway reduction of O_2 and exhibit long-cycle durability. Furthermore, recent research shows that the adsorption and desorption of adsorbates on the catalyst surface in iron–nitrogen co-doped carbon-based catalysts is enhanced due to the unique electronic Fe–N–C bond structures. It has a favourable impact on surface stability and catalyst activity, and exhibits an anti-poisoning effect in fuel cells.[19,20] On the other hand, some reports show iron oxides embedded in carbon matrices that selectively catalyze the $2e^-$ pathway of the ORR.[21–23] Additionally, Fe single-atom coordinated oxidized carbon nanotubes have shown high activity (>90%) in the selective $2e^-$ ORR in neutral electrolytes.[24] Understanding the mechanisms behind selectivity is still a central issue in designing catalysts.[25]

An essential aspect for commercial application in electrocatalytic systems are the fabrication costs of the electrodes. In the past few years, laser-assisted processing methods of low-cost starting materials have been widely investigated for applied electrocatalytic systems. For instance, in 2017, a laser-carbonized membrane was demonstrated as an efficient electrode for water-splitting to produce both H_2 and O_2.[26] In 2018, O_2-plasma treatment of the surface of such laser-carbonized membranes was proven to increase the density of oxygen functional groups as active sites, which reduces the activation energy by facilitating adsorption of OER intermediates.[27] Therefore, in addition to high electrocatalytic activity, the simple and low-energy-consumption preparation method of the electrode has attracted extensive attention.

Here, we report the laser-assisted synthesis of a carbon-supported mixed valence iron oxide-based ORR catalyst. We use citric acid and urea as molecular precursors to create a carbon network-forming agent (CNFA) for laser-assisted carbonization and iron(III) nitrate as a precursor for the *in situ* formation of iron-containing nanoparticles in a laser-patterned nitrogen-doped carbon (LP-NC) matrix. By selection of the synthesis route, the structure of the composite is varied and the ORR selectivity is tuned between the $2e^-$ and $4e^-$ pathways. Comprehensive complementary analysis by X-ray photoelectron spectroscopy (XPS) and high-resolution transmission electron microscopy (HRTEM) suggests the kinetic formation of catalytically active mixed valence iron oxide nanoparticles of different compositions depending on the synthesis route. Their formation mechanism *via* laser-induced carbothermal reduction also influences the local graphitization of the LP-NC matrix surrounding the mixed valence iron oxide nanoparticles.

Results and discussion

Sample preparation and characterization

Laser-patterned catalyst electrodes were fabricated by a two-step approach including ink preparation and laser-carbonization. The inks were prepared by two different routes as illustrated in Fig. 1. In route 1, all molecular precursors, namely citric acid, urea, and $Fe(NO_3)_3$ were thoroughly mixed and then pre-carbonized at 300 °C for 2 h (see the Experimental section). The resulting iron-containing carbon network-forming agents (CNFA(Fe)) with different iron contents were then processed into inks. In route 2, different amounts of $Fe(NO_3)_3$ were added to the readily prepared iron-free CNFA and further processed to inks. As a standard solvent for all inks, ethylene glycol was used. The inks were doctor-bladed on the substrates (PET, Si wafer, or carbon cloth) and dried to obtain films with mean thicknesses of ~30 μm. Then the dry films were irradiated with a mid-infrared CO_2-laser (λ = 10.6 μm) to create homogeneous electrode films in the desired dimensions. The resulting iron-containing LP-NC electrodes are named LP-NC(Fe)_*n*(*x*) with *n* indicating the preparation route (1 or 2) and *x* indicating the mass percentage of Fe after laser-carbonization. The mass percentages of iron in the laser-patterned films were determined by inductively coupled plasma mass spectrometry (ICP-MS) and are listed in Table 1.

In accordance with previous observations, laser-induced carbonization causes a drastic increase in the carbon content at the expense of nitrogen and oxygen (Table S1†). The quantitative iron content is slightly increased after laser treatment. For example, the carbon and iron contents of 48 wt% and 2.3 wt% in CNFA(Fe)_(2.3) increased to 78 wt% and 3 wt% in LP-NC(Fe)_1(3.0) after laser carbonization (Table S1†), respectively. The addition of iron nitrate seems to have no significant influence on the formation of the typical disordered, porous morphology of the films with a relatively low iron content. Only in route 1 at higher concentrations of Fe, *e.g.* 12.1 wt%, the morphology of LP-NC(Fe)_1(12.1) is considerably different compared to that of the films with lower Fe concentrations in terms of forming a somewhat crumpled structure. In comparison, no such impact on the morphology upon addition of iron nitrate is observed for the films prepared by route 2.

The Raman spectra of the films prepared by following route 1, *i.e.* LP-NC(Fe)_1(*x*), show relatively sharp D-, G-, and G′-bands at 1340, 1574, and 2676 cm^{-1}, respectively, and negligible contributions from disorder-induced carbon and sp^3-carbon (D3 at 1460 cm^{-1} and D4 at 1200 cm^{-1}), indicating the formation of a turbostratic graphitic material with a high degree of carbonization.[28,29] With the increasing iron content an increase in the defect related D-band is observed. The same principal observation is also made in the films prepared by following route 2. However, all LP-NC(Fe)_2(*x*) films show large contributions of D3 and D4 peaks as well as a low and broad G′ band. This is generally attributed to samples with a lower degree of graphitization. Iron-based compounds are well-known as catalysts for graphitization of carbon.[30] The mechanism of graphitization is often not clear; however, in this case we observe an obvious difference between the two preparation routes. During pre-carbonization at 300 °C partial decomposition and cross-linking of the molecular precursors occur. Adding $Fe(NO_3)_3$ to the molecular precursors prior to pre-carbonization supports the formation of an iron-containing CNFA(Fe), in which Fe^{3+} is present during the cross-linking, and is thus homogeneously incorporated by coordination (Fig. S1†). On the other hand, the

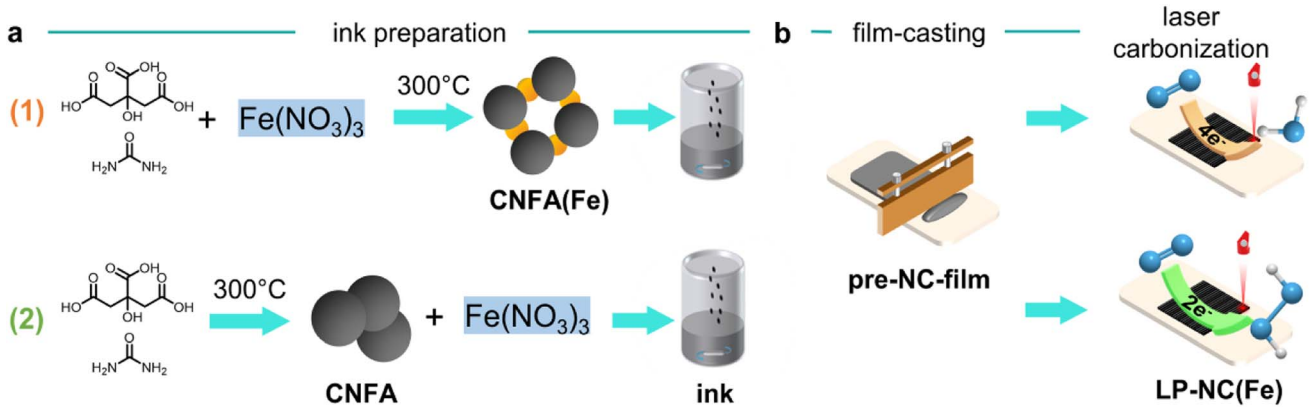

Fig. 1 Illustration of the sample preparation *via* two routes. (a) Route 1: mixtures of citric acid, urea, and $Fe(NO_3)_3$ are pre-carbonized at 300 °C and the resulting CNFA(Fe) is processed to an ink; Route 2: citric acid and urea are pre-carbonized at 300 °C and $Fe(NO_3)_3$ is added to the CNFA and processed to an ink; (b) casting of the CNFA films on substrates and laser-patterning of the films.

Table 1 Overview of the samples. The upper half was prepared according to route 1 and the lower half was prepared according to route 2

	Sample, LP-NC(Fe)_$n(x)$	Citric acid, g	Urea, g	$Fe(NO_3)_3 \cdot 9H_2O$, g	Fe content (ICP), %
Route 1	LP-NC(Fe)_1(3.0)	5	5	0.2	3.0
	LP-NC(Fe)_1(4.6)	5	5	0.3	4.6
	LP-NC(Fe)_1(12.1)	5	5	1	12.1
		CNFA, g		$Fe(NO_3)_3 \cdot 9H_2O$, g	Fe content (ICP), %
Route 2	LP-NC(Fe)_2(3.3)	0.2		0.02	3.3
	LP-NC(Fe)_2(3.8)	0.2		0.04	3.8
	LP-NC(Fe)_2(14.5)	0.2		0.1	14.5

iron-free CNFA used in route 2 is cross-linked before $Fe(NO_3)_3$ is added. As a result, the *in situ* decomposition of the iron-precursors is affected, which is demonstrated in the different Raman patterns, on the one hand, and different electrical conductivities, on the other. In route 1, LP-NC(Fe)_1(3.0) exhibits the highest electrical conductivity with 7.8 S cm^{-1} and decreases with the higher iron content (Fig. S2†)., whereas for route 2 the opposite trend is observed, namely LP-NC(Fe)_2(3.3) with a lower iron content has a lower electrical conductivity of 3.5 S cm^{-1}, which increases to 8.7 S cm^{-1} for higher iron contents LP-NC(Fe)_2(14.5).

Further support for this interpretation is found in the XRD patterns of the films, as we observe narrower graphitic (200) and (10) reflections at 26 and 44° 2Θ for samples prepared by route 1 (Fig. 2e–f). Interestingly, the (10) reflection increases in intensity with the increasing iron concentration, indicating an increase in defects and a change in the lateral size of the graphitic domains.[31] This suggests that an optimal amount of iron is necessary to achieve a high degree of graphitization. Additional peaks at 30.0, 35.4, 43.0, 53.4, 56.9 and 62.5° that appear in the film with the highest iron concentration LP-NC(Fe)_1(12.1) are assigned to the (220), (311), (400), (422), (511), and (440) crystal planes of Fe_3O_4 [ICDD 19-629], respectively. These peaks are not detected in the samples with lower iron concentrations, most likely due to a too small size and too low concentrations of iron-containing nanoparticles.

As a reference, for the primary films of route 1, only graphitic reflection with no signals of iron oxides is observed (Fig. S4†). This indicates that iron oxide is formed during laser-carbonization and not during pre-carbonization. This is also reflected in reference measurements using TEM/EDX analysis, where no iron oxide particles are found in the primary films (Fig. S4†).

In the XRD patterns of the samples prepared by route 2 (Fig. 2f), *e.g.* LP-NC(Fe)_2(14.5), the diffraction peaks at 35.6, and 49.5° correspond to the (110) and (024) lattice planes of Fe_2O_3 (ICDD 33-664) and those at 35.4 and 43.0° are assigned to the (311) and (400) crystal planes of Fe_3O_4. Again, for LP-NC(Fe)_2(3.3) with a lower Fe content, only the graphitic reflection (002) and the carbon (111) symmetric Bragg reflection are observed. Therefore, we conclude that the addition of iron nitrate in different routes not only affects the final oxidation form of iron but also the degree of graphitization and the local crystal structure of the LP-NC.

To study the bonding structure of the materials, X-ray photoelectron spectra (XPS) of all LP-NCs as well as the primary

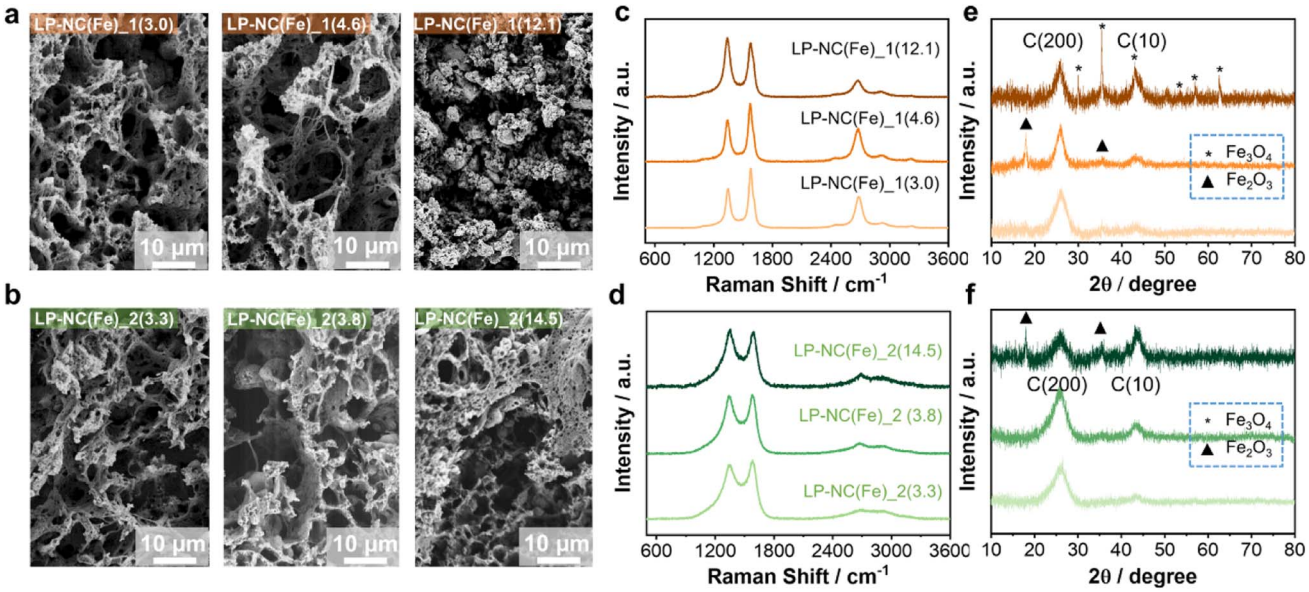

Fig. 2 (a) SEM images of films of LP-NC(Fe)_1(*x*) prepared on a flexible PET substrate by following route 1 and (b) LP-NC(Fe)_2(*x*) prepared by following route 2; (c) corresponding Raman spectra of LP-NC(Fe)_1(*x*) samples prepared by following route 1 and (d) route 2; (e) corresponding X-ray powder diffraction (XRD) patterns of the LP-NC(Fe)_1(*x*) films prepared by following route 1 and (f) route 2.

films with a focus on the C_{1s}, N_{1s}, O_{1s}, and Fe_{2p} regions were collected (Fig. S5–S9†). The C_{1s} region of all LP-NCs reveals a high degree of carbonization reflected by the prominent sp^2-carbon peak at 284.4 eV and the presence of oxygen and nitrogen-containing functional groups indicated by the peaks at 285.3, 286.2 and 287.9 eV which are assigned to sp^3-carbon, C–N/C–O, and C=N/C=O, respectively. The N_{1s} areas of LP-NCs from both route 1 and route 2 show a prominent signal at 399.8 eV stemming from pyrrolic N and two minor peaks at 398.5 and 401.5 eV from pyridinic and graphitic N, respectively. In the primary films, pyridinic N is the major peak (Fig. S7†).

An important difference between the primary films of route 1 and route 2 (pre_NC(Fe)_1(*x*) and pre_NC(Fe)_2(*x*)) is found in the N_{1s} region. The pre_NC(Fe)_2(*x*) films (route 2) show an additional peak at 406.5 eV corresponding to NO_3^- (Fig. S9†), while it is not present in pre_NC(Fe)_1(*x*) (route 1). This indicates that in route 1, iron nitrate is decomposed after pre-carbonization. The O_{1s} regions of the samples show peaks originating in oxygen functional groups from the carbon matrix, as well as an iron oxide related peak at 530.1 eV (Fig. S6 and S9†). The intensity of this peak increases with an increase in the iron content coming from the formation of iron oxide.

For the Fe_{2p} region of route 2, in the primary film pre-NC(Fe)_2(3.3), the peaks at 710.3 eV and 723.4 eV constitute the characteristic doublet of Fe $2P_{3/2}$ and $2P_{1/2}$ core-level spectra of Fe^{3+} are observed due to the addition of iron nitrate (Fig. 3a). After laser-carbonization, the spectra of LP-NC(Fe)_2(3.3) shows an additional Fe(0) peak at 706.8 and the peaks shift to high binding energy and broaden, which is typically assigned to the co-presence of Fe^{3+} and Fe^{2+} species.[32,33] In contrast, for LP-NC(Fe)_1(3.0), in addition to the Fe(0) peak, the levels $Fe^{3+}(2P_{3/2})$ and $Fe^{3+}(2P_{1/2})$ and their satellite peak at around 719.5 eV are characteristic of Fe_2O_3. However, the peaks observed in the primary film pre-NC(Fe)_1(3.0) shift to low binding energy and the peaks appearing at 709.5 eV and 722.6 eV are assigned to $Fe^{2+}(2P_{3/2})$ and $Fe^{2+}(2P_{1/2})$, respectively. Interestingly, from the elemental composition quantified by using the XPS spectra (Table S2†), the iron content on the surface of the LP-NC(Fe)_2(*x*) films of route 2 is significantly higher than that of route 1.

The two samples with low iron contents, LP-NC(Fe)_1(3.0) and LP-NC(Fe)_2(3.3), were investigated using (scanning) transmission electron microscopy ((S)TEM) and energy-dispersive X-ray (EDX) microanalysis (Fig. 3b). In both samples iron-containing nanoparticles are embedded in a carbonized matrix; however, the type of the crystalline phase formed during the synthesis and the overall distributions of the particles in the matrix are found to be different. In the LP-NC(Fe)_2(3.3) sample we observed a local increase in the degree of graphitization of the carbonized matrix around the iron-containing particles, forming a "graphitic" shell. In contrast, in LP-NC(Fe)_1(3.0) the carbon film displayed uniform graphitization throughout all analyzed areas (Fig. 3c). This observation is in good agreement with the Raman data presented above, showing that LP-NC(Fe)_1(3.0) exhibits a higher degree of graphitization. Analysis of fast Fourier transforms (FFTs) obtained from the HRTEM images of iron-containing nanoparticles suggests that these two samples contain different forms of iron oxides. LP-NC(Fe)_1(3.0) has η-Fe_2O_3 particles (orthorhombic unit cell, sp.gr. *Cmcm*), while in LP-NC(Fe)_2(3.3) α-Fe_2O_3 particles (trigonal unit cell, sp.gr. $R\bar{3}c$) and FeO particles (cubic unit cell, $Fm\bar{3}m$) were observed. In general, the LP-NC(Fe)_2(3.3) sample was found to be less homogeneous, showing, in addition to nanoparticles, large Fe–O-containing flakes as well as very small Fe-containing clusters (Fig. S11†). Local EDX analysis performed on both samples

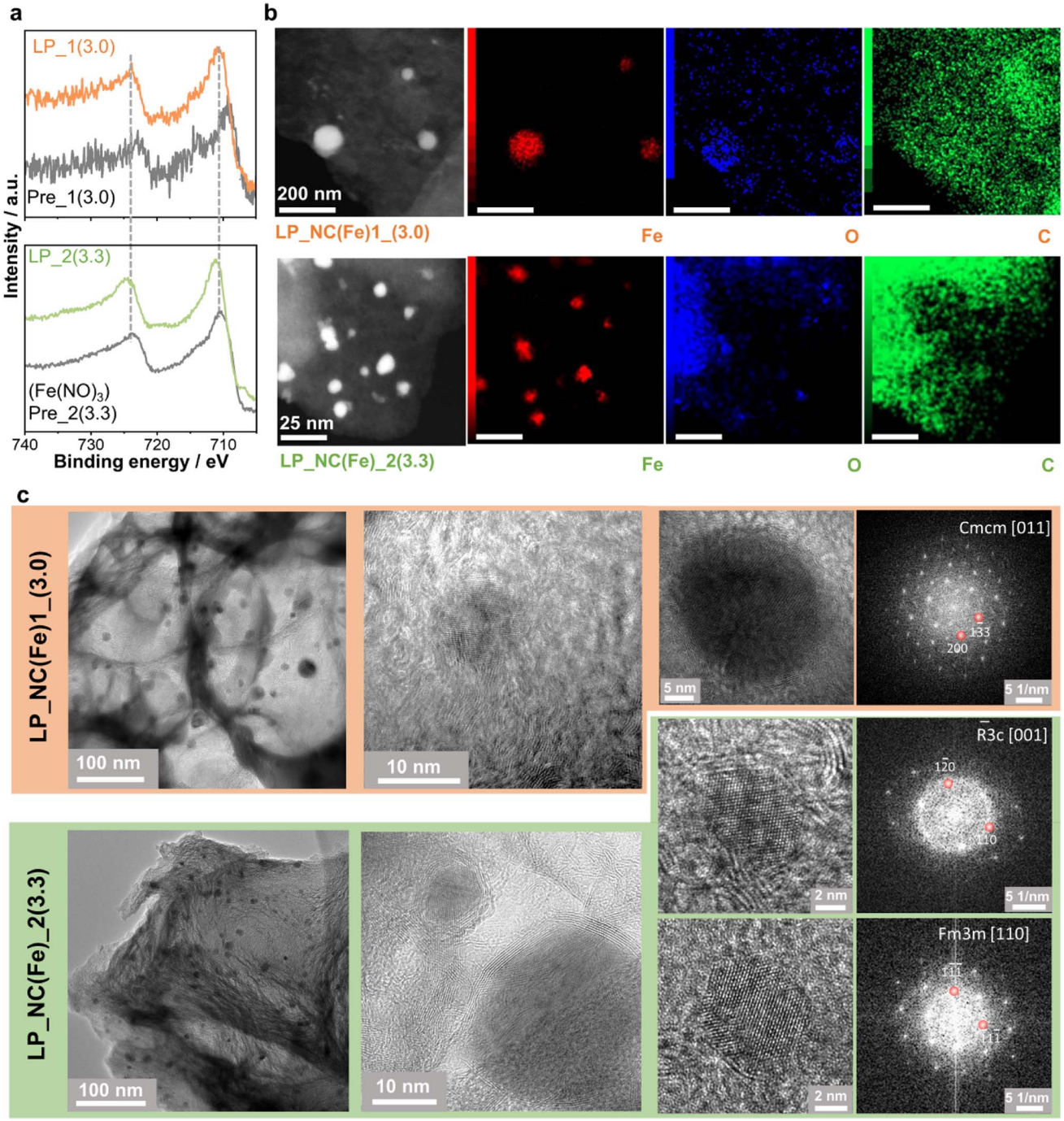

Fig. 3 (a) Fe_{2p} regions of the XPS spectra of LP_NC(Fe)_1(3.0)/pre_NC(Fe)_1(3.0) (top) and LP_NC(Fe)_2(3.3)/pre_NC(Fe)_2(3.3) (bottom); (b) ADF-STEM images and the corresponding EDX maps of Fe-Kα, O–K, and C–K signals in LP_NC(Fe)_1(3.0) (top) and LP_NC(Fe)_2(3.3) (bottom) samples. The corresponding EDX spectra are shown in Fig. S10;† (c) overview TEM images and HRTEM images of Fe-containing nanoparticles in LP_NC(Fe)_1(3.0) (orange) and LP_NC(Fe)_2(3.3) (green). Fast Fourier transforms obtained from HRTEM images of the particles are shown on the right.

confirms that nanoparticles contain Fe and O; however, since oxygen is partially present in the carbonized matrix, direct determination of the phase composition from EDX maps is not always possible. Moreover, one can see variations of the contrast in annular-dark field STEM (ADF-STEM) images (Fig. 3a) and in the oxygen distribution in the O–K maps, suggesting that the oxygen content can vary even within the same particle. Overall, the TEM and EDX data are in line with XPS measurements, suggesting that *via* route 1 Fe_2O_3 oxide is predominantly formed, while route 2 leads to the formation of both Fe_2O_3 and FeO.[34] The intrinsic inhomogeneity among the

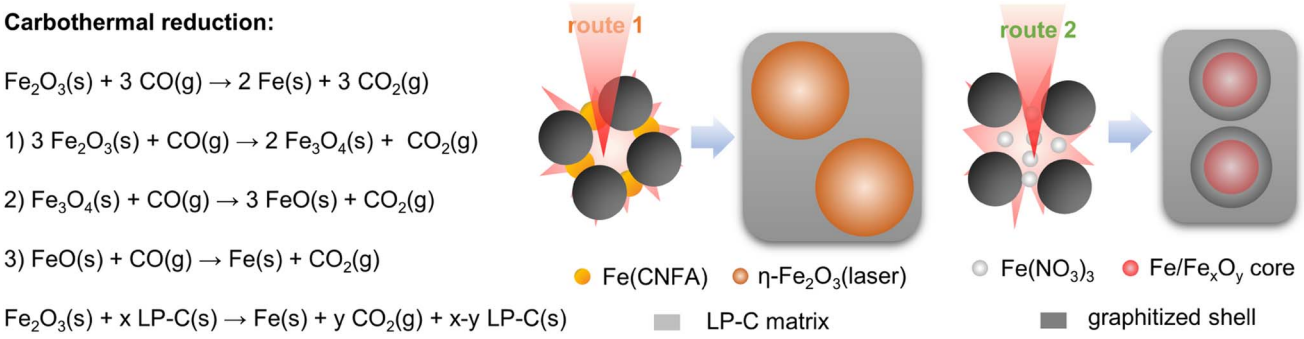

Fig. 4 Carbothermal reduction mechanisms and illustration of the formation of iron containing particles embedded into the LP-NC matrix in route 1 and route 2.

particles found by EDX can be the reason for the small but distinct signal of Fe(0) observed in the XPS spectra (Fig. S11†).

Proposed formation mechanism

Taking the results of the previous characterization investigations into consideration, we propose the formation mechanism based on carbonization of the CNFA and simultaneous carbothermal reduction of the iron precursors (Fig. 4). Typically, during such carbothermal reductions, which occur in the temperature range of up to 1000 °C, the carbon is oxidized and cleaves off CO or CO_2, which subsequently supports the graphitization of the remaining carbon.[35,36] Notably, the reaction temperature cannot be measured directly. However, by the degree of graphitization a reaction temperature gradient of <500 °C and >1500 °C between the lower and the upper layer of the LP-NC film is assumed.[37] The difference between the two routes lies in the prearrangement and the nature of the iron precursors in the primary inks.

For route 1, at temperatures >80 °C urea decomposes into isocyanate and ammonia which reacts with iron nitrate to generate coordinated Fe^{3+} species (see XPS) and potentially FeO(OH).[38] These Fe^{3+} species are expected to be incorporated homogeneously into the cross-linked CNFA. In a previous study, we demonstrate that upon annealing a mixture of citric acid and urea, two main intermediate products are formed, namely HPPT and oligomeric urea.[39] These two components form strong hydrogen-bond networks which eventually cross-link at elevated temperatures to form aggregated particles. The Fe^{3+} species are found homogeneously inside these particles (Fig. S4†). A recrystallization into α-Fe_2O_3, as it has been observed in other studies at ~300 °C, cannot be confirmed.[40–42] Although, the decomposition of iron nitrate during pre-carbonization (Fig. S7†) is confirmed, no iron oxide nanoparticles were identified in XRD (Fig. S3†) or TEM (Fig. S4†) analysis. The involvement of Fe^{3+} species in the process of cross-linking during pre-carbonization may enhance thermal stability and electrical conductivity of the resulting LP-NC network, which is observed from the XPS spectra (Fig. 3) of pre-NC(Fe)_1(x) where the peaks shift to a lower binding energy. During laser-carbonization the cross-linked pre-NC(Fe)_1(x) form a homogeneous graphitized carbon matrix with predominantly η-Fe_2O_3 particles incorporated.

On the other hand, in route 2, $Fe(NO)_3$ is added after cross-linking and does not influence the cross-linking of the CNFA. The transformation from $Fe(NO)_3$ into iron-containing nanoparticles occurs during laser-treatment on a short kinetic timescale. The effect of the carbothermal reduction is apparent by the formation of the graphitic shells around the iron-containing particles (Fig. 3c). This shift of thermal energy during the laser treatment leads to the localized graphitic domains while larger fractions of the carbon network are still amorphous, which explains the presence of D3 and D4 bands in the Raman spectra (Fig. 2d). In general, higher concentrations of iron precursors foster the formation of larger iron oxide particles which are detected in XRD, while the small particle sizes of <20 nm at low concentrations do not afford sharp peaks.

Electrocatalytic ORR performance

The performance of the LP-NC(Fe)_1(x) and LP-NC(Fe)_2(x) composite materials was evaluated as ORR electrocatalysts in alkaline media (0.1 M KOH) using a rotating ring disk electrode (RRDE) set up. The analysis was performed using a glassy carbon RRDE tip with a platinum ring (see the Experimental section). A slurry prepared using ground materials with Nafion as a binder was drop cast on the tip. The larger current densities reached with LP-NC(Fe)_1(x) samples compared to that with LP-NC(Fe)_2(x) in the linear sweep voltammetry curves (Fig. 5) are indicative for higher activity and local conductivity of the samples (Fig. S2†) and could be explained by the higher graphitization of the catalyst. The number of electrons transferred during the reduction reaction was calculated based on the amount of H_2O_2 detected at the Pt ring. LP-NC(Fe)_1(x) samples clearly promote the reduction of oxygen mainly through a $4e^-$ transfer mechanism but, at lower iron loadings a certain contribution of the $2e^-$ transfer mechanism is observed. On the other hand, O_2 is reduced through a $2e^-$ transfer by LP-C(Fe)_2(3.3) and through a $4e^-$ transfer mechanism by sample LP-C(Fe)_2(14.5).

There are many properties which influence the performance and mechanism of a sample as a catalyst in the ORR, such as conductivity, structure and functional groups of the carbon matrix as well as the presence of metallic particles. Due to this fact, it is not easy to pinpoint the exact catalytic site and clearly state a cause for the main difference between samples. Samples

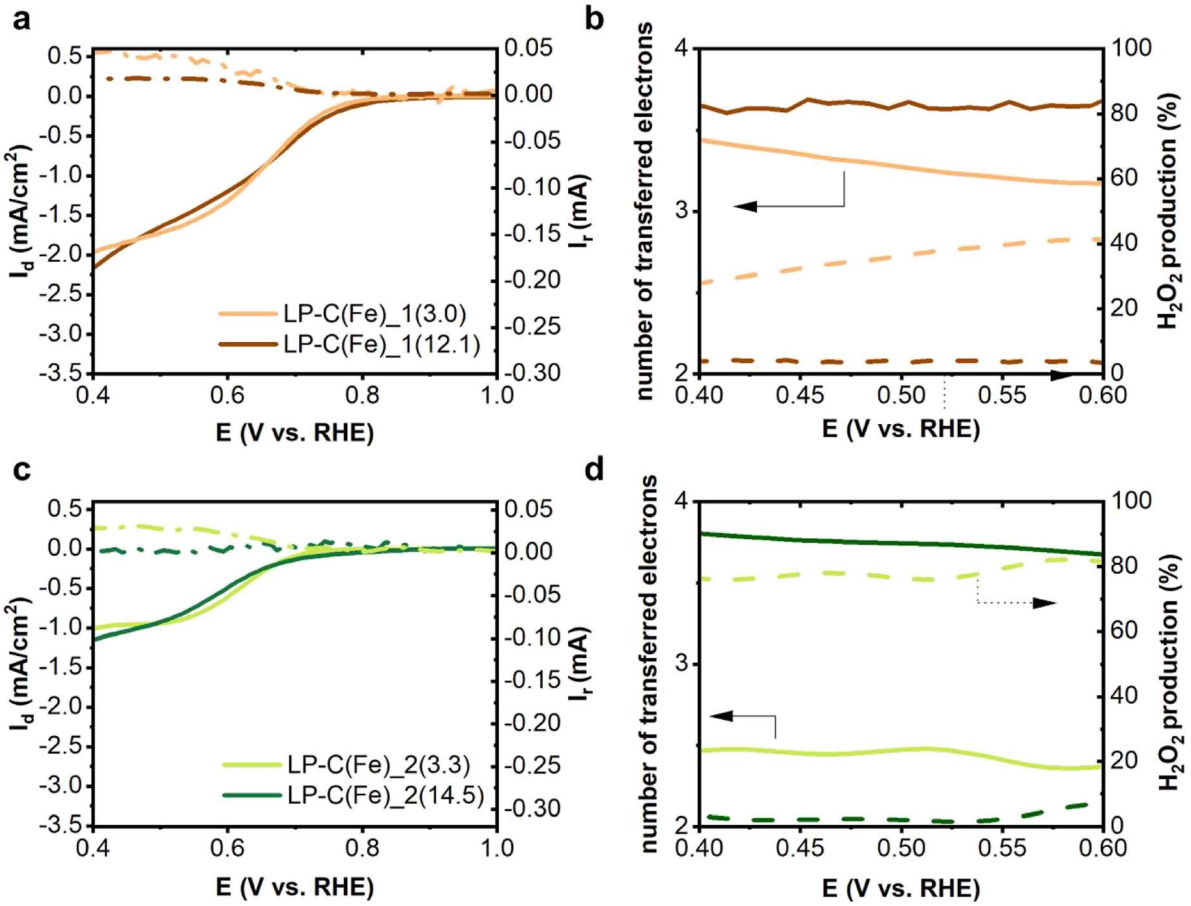

Fig. 5 ORR performance in oxygen saturated 0.1 M KOH evaluated using an RRDE setup. (a) Linear sweep voltammetry and (b) calculated number of transferred electrons and H_2O_2 production efficiency of LP-NC(Fe)_1(3.0), LP-NC(Fe)_1(4.6), and LP-NC(Fe)_1(12.1); (c) linear sweep voltammetry and (d) calculated number of transferred electrons and H_2O_2 production efficiency of LP-NC(Fe)_1(3.3), and LP-NC(Fe)_1(14.5). H_2O_2 ring current and selectivity (%) are in dashed lines.

prepared by route 1 are more conductive which enhances the current densities. The difference in conductivity may facilitate the electron transfer and favour the 4e$^-$ transfer mechanism.

Another property that needs to be addressed is the nitrogen species. Importantly, the samples LP-C(Fe)_1(3.0) and LP-C(Fe)_2(3.3) contain mainly pyrrolic nitrogen and show relatively high H_2O_2 production efficiency (Table S3†). The role of pyrrolic nitrogen in selective H_2O_2 production was well demonstrated by Yang *et al.* in a report on low-cost N-doped carbon catalysts fabricated in a one-step carbonization of pomelo peel biomass waste.[43] Furthermore, Li *et al.* have shown that an increase in the content of pyrrolic nitrogen leads to a higher production of H_2O_2, which they further supported by X-ray absorption near-edge structure spectroscopy (XANES) analysis.[44] When looking at our XPS analysis, it was found that the content of pyrrolic nitrogen compared to that of other nitrogen types is higher for samples from route 2, which supports the 2e$^-$ mechanism. Pyrrolic nitrogen is dominant in both sets of samples, and might have a larger influence as a catalytic site at lower iron loadings. This goes along with the certain contribution of the 2e$^-$ mechanism observed for samples LP-NC(Fe)_1(3.0) and LP-NC(Fe)_2(3.3).

The studies on carbon-based materials that contain iron oxide do not show a clear correlation between the type of iron oxide and the resulting mechanism and a through literature survey is presented in Table S4.† We observed a clear difference in the nature of the iron oxides present in our materials as summarized in Table 2. In the case of LP-NC(Fe)_1(x), the iron oxide is distributed on an evenly carbonised matrix, meaning that the iron oxide will be directly in contact with the electrolyte. In the case of LP-NC(Fe)_2(x), the iron oxide nanoparticles are surrounded by a graphitic layer, which prevents direct exposure to the electrolyte. This will change the active site and will have an effect on the desorption of the –OOH intermediate, which might lead to a different mechanism. We observed that for both sets of samples the performance of the electrocatalysts towards the 4e$^-$ mechanism is enhanced at larger iron loadings. At larger loadings, the formation of larger carbon graphitic domains is more favourable which might facilitate the electron transfer. The iron catalytic sites from route 1 are exposed to the electrolyte and the support conductivity favours that, even at low iron loadings, the contribution of the 4e$^-$ transfer mechanism predominates. On the other hand, in samples from route 2 the sites are not directly exposed to the electrolyte and the

Table 2 Summary of the results obtained using the materials as oxygen reduction reaction electrocatalysts

		n^a	H_2O_2 production		
Sample	Onset E^b, V	pH = 14[b]	pH = 14[b]	pH = 7.2[c]	Fe type
LP-NC(Fe)_1(3.0)	0.77	3.5	40%	10%	η-Fe_2O_3 and Fe(0)
LP-NC(Fe)_1(12.1)	0.80	4	2%	—	Fe_3O_4
LP-NC(Fe)_2(3.3)	0.70	2.5	80%	3%	α-Fe_2O_3, FeO, and Fe(0)
LP-NC(Fe)_2(14.5)	0.72	3.5	8%	—	α-Fe_2O_3

[a] Number of transferred electrons. [b] 0.1 M KOH as an electrolyte. [c] Phosphate buffer as an electrolyte.

carbon support is not as conductive. Thus, at a low iron content, the $2e^-$ mechanism predominates due to the contribution of the pyrrolic functional groups and the poorer conductivity. When the loading of iron increases, the contribution of the $4e^-$ transfer mechanism also does. We also analysed the behaviour of samples LP-C(Fe)_2(3.8) in order to further corroborate this hypothesis (Fig. S12†). The results show that when the iron content is between that of samples LP-C(Fe)_2(3.3) and LP-C(Fe)_2(14.5), the contribution of both mechanisms is also in between. For instance, the average number of electrons transferred is 3 and the average percentage of H_2O_2 produced is 50%.

Samples LP-C(Fe)_1(3.0) and LP-C(Fe)_2(3.3) were also evaluated in O_2-saturated neutral media (500 mM phosphate buffer with pH 7.2). In this electrolyte, the onset of the ORR is at 0.5 V *vs.* RHE in both cases. Both samples yield very little H_2O_2 and the number of transferred electrons is above 3 (Fig. S13†). The limiting current obtained was much larger than that found in basic media.

Conclusions

In summary, we introduced a concept to fabricate ORR catalyst electrodes by a simple and cost-effective laser-assisted carbonization method affording mixed valence iron oxide nanoparticles embedded in a nitrogen-doped carbon matrix. The electrodes are based on earth-abundant and recyclable materials and are processed by an efficient, fast and low-energy synthesis method. By simply changing the preparation sequence we were able to modulate the catalyst performance between the $2e^-$ and $4e^-$ pathways and thereby create product selectivity in the ORR. Our experimental results demonstrate how different iron contents and the sequence of the film preparation influence the chemical and structural composition of the active catalysts, namely the type of iron oxide, the degree of graphitization, and the local structure of the final laser-carbonized electrodes. The effect of the type of nitrogen functionality, degree of graphitization and iron type was used to rationalize the ORR performance of the samples. The obtained mixed valence iron oxide structures, namely 3 wt% α-Fe_2O_3/FeO/Fe embedded into N-pyrrolic doped carbons were identified as highly active and selective for O_2 reduction to H_2O_2. Well graphitized LP-NC with predominant η-Fe_2O_3/Fe species embedded preferably supports the $4e^-$ pathway to generate H_2O with 4% and 10% efficiency in alkaline or neutral electrolyte, respectively. Future efforts can be focused on the electrode design for pure H_2O generation and the utilization of alternative carbon-network forming agents or precursors for the selective formation of catalytically active interfaces. Such electrodes may find application as environmentally friendly and sustainable alternatives in, for example, energy storage, water treatment, and H_2O_2 generation.

Experimental section

Materials

Citric acid (>99%, Sigman-Aldrich), urea (>99.3%, Alfa Aesar), iron(III) nitrate nonahydrate (>98%, Alfa Aesar), ethylene glycol (≥99.7%, AnalaR Normapur, VWR chemicals), polyvinylpyrrolidone (average mol wt. 10 000, Sigma-Aldrich), 0.1 M Titripur® potassium hydroxide solution (Aldrich), Nafion 117 5% solution (Aldrich) and pH 7 phosphate buffer solution (500 mM, Aldrich) were used.

Preparation of LP-NC(Fe)_*n*(*x*)

Route 1. 5 g citric acid, 5 g urea and 0.2, 0.3, or 1.0 g iron(III) nitrate nonahydrate ($Fe(NO_3)_3 \cdot 9H_2O$) were dissolved in 10 mL methanol and thoroughly mixed. The solvent was evaporated and the solid mixture was annealed at 300 °C for 2 h in a tube furnace at a heating rate of 3.11 K min^{-1}. The resulting black powders were ground by ball milling (PM 100, Retsch) for 1 h at 650 rpm to obtain the iron doped carbon network-forming agents (CNFA(Fe)). 0.2 g of each CNFA(Fe) were then dispersed in 2 mL of ethylene glycol and stirred for 24 h to obtain viscous inks.

Route 2. The CNFA (CA/U(300)) was prepared according to route 1 without the addition of $Fe(NO_3)_3 \cdot 9H_2O$.[45] $Fe(NO_3)_3 \cdot 9H_2O$ was dissolved in 0.2 mL ethylene glycol to obtain solutions with different concentrations between 0.1 and 0.5 g mL^{-1}. 0.2 g of CA/U(300) was then added and the mixture was stirred for 24 h to obtain a viscous ink.

A drop of the ink was applied onto the substrate (PET) and the ink was doctor bladed with a blade distance of 130 μm. Ethylene glycol was then evaporated at 80 °C on a precision hotplate (PZ2860-SR, Gestigkeit GmbH) to obtain the final films with mean thicknesses of 30 μm.

The powder collection of the sample. A drop of the ink was applied onto a Si wafer and then doctor bladed with a blade distance of 700 μm. Ethylene glycol was evaporated at 80 °C on a hotplate. After laser-carbonization, the powder of LP-NC(Fe)

was scraped off the silicon wafer. The powders were thoroughly washed with 1.0 M NaOH by sequential sonication and centrifugation until the supernatant was clear, *i.e.* all unconverted precursors were washed out. The remaining black solid was washed with H_2O and methanol to remove all NaOH and obtain a pure laser-carbonized product.

A high-precision laser engraver setup (Trotec Speedy 100, 60 W CO_2-laser, 2.5 inch focus lens, and a spot size of 170 μm) was used for laser-carbonization. The resulting energy fluence ($F = 72$ J m^{-1}) was calculated from the product of the laser power ($P = 1.02$ W) and the scanning speed (71 s m^{-1}). Each laser pattern consists of 100 parallel laser lines with a length of 10 mm and a line separation of 0.1 mm to obtain a homogeneous electrode film of 10 × 10 mm.

Characterization

Raman spectra were obtained with a confocal Raman microscope (alpha300, WITec, Germany) equipped with a piezo-scanner (P-500, Physik Instrumente, Karlsruhe, Germany). The laser, $\lambda = 532$ nm, was focused on the samples through a 50× objective. The laser power on the sample was set to 5.0 mW. Scanning electron microscopy was performed on a Zeiss LEO 1550-Gemini system (acceleration voltage: 3 to 10 kV). An Oxford Instruments X-MAX 80 mm^2 detector was used to collect the SEM-EDX data. Transmission electron microscopy (TEM) was performed using a double Cs corrected JEOL JEM-ARM200F (S)TEM operated at 80 kV, 10 μA and equipped with a cold-field emission gun and a high-angle silicon drift energy dispersive X-ray (EDX) detector (solid angle up to 0.98 steradians with a detection area of 100 mm^2). Annular dark field scanning transmission electron microscopy (ADF-STEM) images were collected at a probe convergence semi-angle of 25 mrad. The so-called "beam shower" procedure was performed with a defocused beam at a magnification of 8000× for 30 minutes; it was necessary for reducing hydrocarbon contamination during subsequent imaging at high magnification. To prepare the TEM samples, the carbon material has been dispersed in methanol, sonicated for 10 min, drop cast on a lacey carbon TEM grid and dried at room temperature. Elemental combustion analysis was performed with a vario MICRO cube CHNOS elemental analyzer (Elementar Analysensysteme GmbH). The elements were detected with a thermal conductivity detector (TCD) for C, H, N and O and an infrared (IR) detector for sulphur. Inductively coupled plasma mass spectrometry (ICP-MS) was performed with a PerkinElmer ICP-OES Optima 8000. The sample preparation: 10 mg powder of the sample was added into the ICP tube, followed by 167 μL conc. HNO_3 and 333 μL conc. HCl. X-ray diffraction was performed on a Bruker D8 Advance diffractometer in the Bragg–Brentano mode at the Cu Kα wavelength. XPS measurements were performed on a ThermoScientific Escalab 250 Xi. A micro-focused, monochromated AlKα X-ray source (1486.68 eV) and a 400 μm spot size were used in the analysis. Samples were prepared using carbon tape. Calibration was performed according to the sp^2 peak in each sample. CasaXPS software was used to analyze the resulting spectra. Electrochemical tests were performed using a rotating ring disk electrode (RRDE) purchased from PINE and Interface 1000 and Interface 1010 (Gamry) potentiostats. The three-electrode cell setup consisted of an Ag/AgCl electrode as a reference, a Pt wire as a counter electrode and 5 mm glassy carbon (disk)/platinum (ring) RRDE tips modified with the materials as working electrodes. It is important to consider that by using Pt rings the number of transferred electrons might be overestimated.[46] To prepare the RRDE tips for measurements, 10 μL of catalyst ink was deposited on the glassy carbon tip and dried at room temperature overnight. The ink is prepared by mixing 50 μL of Nafion 117 solution (5 wt%, purchased by Aldrich), 500 μL of distilled water, 250 μL of isopropanol, and 5 mg powder of laser-carbonized samples as catalysts. Linear sweep voltammetry (LSV) was performed in O_2 saturated 0.1 M KOH solution, or pH 7, 500 mM phosphate buffer, with a scan rate of 10 mV s^{-1} at 1000 rpm rotation speed. The ring was set at a potential of 1.2 V *vs.* RHE to ensure fast oxidation of H_2O_2. The collection efficiency of the ring was calibrated before the measurements following the indication of the RRDE setup provider. The electron transfer number, n, and hydrogen peroxide yield, % H_2O_2, are calculated using eqn (1) and (2).w

$$n = 4 \times \frac{I_d \times N}{I_d \times N + I_r} \quad (1)$$

$$\%H_2O_2 = 100 \times \frac{2 \times I_r}{I_d \times N + I_r} \quad (2)$$

here I_r stands for ring current, I_d for disk current and N for the collection efficiency of the electrodes. The collection efficiency was empirically measured using a ferrocyanide/ferricyanide half-reaction as a single-electron, reversible half-reaction. The rotating ring disc electrodes were placed in 10 mM of potassium ferricyanide ($K_3Fe(CN)_6$) 0.1 M KOH solution and were operated at rotation rates between 500 and 2000 rpm. The potential of the disk electrode was swept from cathodic potentials at 50 mV s^{-1} towards more negative potentials (potential range 0.3 V to −0.75 V *vs.* Ag/AgCl). The potential of the ring electrode was biased at 0.5 V *vs.* Ag/AgCl. The current obtained from the ring when the disk was disconnected was subtracted from I_r. The measured ratio of the ring (anodic) limiting current to the disk (cathodic) limiting current is the empirical collection efficiency. We checked that this number was independent of the rotation rate. We obtained a collection efficiency of 0.21 ± 0.01 for the bare GC, and a collection efficiency of 0.26 ± 0.03 for all electrodes except for electrode LP-C(Fe)_1(3.0) for which the collection efficiency was 0.45 ± 0.05.

Data availability statement

All data needed to evaluate the conclusions in the paper are present in the paper and/or the ESI.† Additional datasets generated during and/or analysed during the current study are available from the corresponding author on reasonable request.

Conflicts of interest

The authors declare that they have no known competing financial interests or personal relationships that could have appeared to influence the work reported in this paper.

Author contributions

Huize Wang: investigation, conceptualization, methodology, validation, writing – original draft; Maria Jerigova: investigation, conceptualization, methodology, validation, writing – original draft; Jing Hou: investigation, conceptualization, methodology, validation, writing – original draft; Nadezda V. Tarakina: conceptualization, methodology, validation, writing – original draft, writing – review & editing, supervision; Nieves López-Salas: conceptualization, methodology, validation, writing – original draft, writing – review & editing, supervision, project administration; Volker Strauss: conceptualization, methodology, validation, writing – original draft, writing – review & editing, supervision, project administration.

Acknowledgements

We gratefully acknowledge funding from the Fonds der Chemischen Industrie and the Max Planck Society and the support from Prof. Markus Antonietti. Open Access funding was provided by the Max Planck Society.

References

1 J. Masa, C. Andronescu and W. Schuhmann, Electrocatalysis as the Nexus for Sustainable Renewable Energy: The Gordian Knot of Activity, Stability, and Selectivity, *Angew. Chem., Int. Ed.*, 2020, **59**, 15298–15312.

2 S. Chu, Y. Cui and N. Liu, The path towards sustainable energy, *Nat. Mater.*, 2016, **16**, 16–22.

3 X. Zhao and Y. Liu, Origin of Selective Production of Hydrogen Peroxide by Electrochemical Oxygen Reduction, *J. Am. Chem. Soc.*, 2021, **143**, 9423–9428.

4 M. Shao, Q. Chang, J. P. Dodelet and R. Chenitz, Recent Advances in Electrocatalysts for Oxygen Reduction Reaction, *Chem. Rev.*, 2016, **116**, 3594–3657.

5 Y.-J. Wang, N. Zhao, B. Fang, H. Li, X. T. Bi and H. Wang, Carbon-Supported Pt-Based Alloy Electrocatalysts for the Oxygen Reduction Reaction in Polymer Electrolyte Membrane Fuel Cells: Particle Size, Shape, and Composition Manipulation and Their Impact to Activity, *Chem. Rev.*, 2015, **115**, 3433–3467.

6 L. Zhang, P. Lu, Y. Luo, J. Y. Zheng, W. Ma, L. X. Ding and H. Wang, Graphene-quantum-dot-composited platinum nanotube arrays as a dual efficient electrocatalyst for the oxygen reduction reaction and methanol electro-oxidation, *J. Mater. Chem. A*, 2021, **9**, 9609–9615.

7 L. Zhang, S. Jiang, W. Ma and Z. Zhou, Oxygen reduction reaction on Pt-based electrocatalysts: four-electron vs. two-electron pathway, *Chin. J. Catal.*, 2022, **43**, 1433–1443.

8 Y. Li, W. Zhou, H. Wang, L. Xie, Y. Liang, F. Wei, J.-C. Idrobo, S. J. Pennycook and H. Dai, An oxygen reduction electrocatalyst based on carbon nanotube–graphene complexes, *Nat. Nanotechnol.*, 2012, **7**, 394–400.

9 Y. L. Zhang, K. Goh, L. Zhao, X. L. Sui, X. F. Gong, J. J. Cai, Q. Y. Zhou, H. Da Zhang, L. Li, F. R. Kong, D. M. Gu and Z. B. Wang, Advanced non-noble materials in bifunctional catalysts for ORR and OER toward aqueous metal–air batteries, *Nanoscale*, 2020, **12**, 21534–21559.

10 Q. Chang, P. Zhang, A. H. B. Mostaghimi, X. Zhao, S. R. Denny, J. H. Lee, H. Gao, Y. Zhang, H. L. Xin, S. Siahrostami, J. G. Chen and Z. Chen, Promoting H2O2 production via 2-electron oxygen reduction by coordinating partially oxidized Pd with defect carbon, *Nat. Commun.*, 2020, **11**, 1–9.

11 G. Gao, Y. Tian, X. Gong, Z. Pan, K. Yang and B. Zong, Advances in the production technology of hydrogen peroxide, *Chin. J. Catal.*, 2020, **41**, 1039–1047.

12 N. Wang, S. Ma, P. Zuo, J. Duan and B. Hou, Recent Progress of Electrochemical Production of Hydrogen Peroxide by Two-Electron Oxygen Reduction Reaction, *Adv. Sci.*, 2021, **8**, 1–26.

13 K. Chen, K. Liu, P. An, H. Li, Y. Lin, J. Hu, C. Jia, J. Fu, H. Li, H. Liu, Z. Lin, W. Li, J. Li, Y.-R. Lu, T.-S. Chan, N. Zhang and M. Liu, Iron phthalocyanine with coordination induced electronic localization to boost oxygen reduction reaction, *Nat. Commun.*, 2020, **11**, 4173.

14 Y. Xue, W. Jin, H. Du, S. Wang, S. Zheng and Y. Zhang, Tuning α-Fe2O3 nanotube arrays for the oxygen reduction reaction in alkaline media, *RSC Adv.*, 2016, **6**, 41878–41884.

15 Z. Xiao, G. Shen, F. Hou, R. Zhang, Y. Li, G. Yuan, L. Pan, J. J. Zou, L. Wang, X. Zhang and G. Li, Highly dispersed γ-Fe2O3 embedded in nitrogen doped carbon for the efficient oxygen reduction reaction, *Catal. Sci. Technol.*, 2019, **9**, 4581–4587.

16 Y. Wang, R. Gan, H. Liu, M. Dirican, C. Wei, C. Ma, J. Shi and X. Zhang, Fe3O4/Fe2O3/Fe nanoparticles anchored on N-doped hierarchically porous carbon nanospheres as a high-efficiency ORR electrocatalyst for rechargeable Zn-air batteries, *J. Mater. Chem. A*, 2021, **9**, 2764–2774.

17 J. Zhu, Z. Xiong, J. Zheng, Z. Luo, G. Zhu, C. Xiao, Z. Meng, Y. Li and K. Luo, Nitrogen-doped graphite encapsulated Fe/Fe3C nanoparticles and carbon black for enhanced performance towards oxygen reduction, *J. Mater. Sci. Technol.*, 2019, **35**, 2543–2551.

18 Z. Schnepp, Y. Zhang, M. J. Hollamby, B. R. Pauw, M. Tanaka, Y. Matsushita and Y. Sakka, Doped-carbon electrocatalysts with trimodal porosity from a homogeneous polypeptide gel, *J. Mater. Chem. A*, 2013, **1**, 13576–13581.

19 Y. Yan, H. Cheng, Z. Qu, R. Yu, F. Liu, Q. Ma, S. Zhao, H. Hu, Y. Cheng, C. Yang, Z. Li, X. Wang, S. Hao, Y. Chen and M. Liu, Recent progress on the synthesis and oxygen reduction applications of Fe-based single-atom and double-atom catalysts, *J. Mater. Chem. A*, 2021, **9**, 19489–19507.

20 H. Shen, T. Thomas, S. A. Rasaki, A. Saad, C. Hu, J. Wang and M. Yang, Oxygen Reduction Reactions of Fe-N-C Catalysts: Current Status and the Way Forward, *Electrochem. Energy Rev.*, 2019, **2**, 252–276.

21 W. R. P. Barros, Q. Wei, G. Zhang, S. Sun, M. R. V Lanza and A. C. Tavares, Oxygen reduction to hydrogen peroxide on Fe3O4 nanoparticles supported on Printex carbon and Graphene, *Electrochim. Acta*, 2015, **162**, 263–270.

22 X. Xu, C. Shi, Q. Li, R. Chen and T. Chen, Fe–N-Doped carbon foam nanosheets with embedded Fe2O3 nanoparticles for highly efficient oxygen reduction in both alkaline and acidic media, *RSC Adv.*, 2017, **7**, 14382–14388.

23 X. Cheng, S. Dou, G. Qin, B. Wang, P. Yan, T. T. Isimjan and X. Yang, Rational design of highly selective nitrogen-doped Fe2O3-CNTs catalyst towards H2O2 generation in alkaline media, *Int. J. Hydrogen Energy*, 2020, **45**, 6128–6137.

24 K. Jiang, S. Back, A. J. Akey, C. Xia, Y. Hu, W. Liang, D. Schaak, E. Stavitski, J. K. Nørskov, S. Siahrostami and H. Wang, Highly selective oxygen reduction to hydrogen peroxide on transition metal single atom coordination, *Nat. Commun.*, 2019, **10**, 3997.

25 B. Wu, H. Meng, D. M. Morales, F. Zeng, J. Zhu, B. Wang, M. Risch, Z. J. Xu and T. Petit, Nitrogen-Rich Carbonaceous Materials for Advanced Oxygen Electrocatalysis: Synthesis, Characterization, and Activity of Nitrogen Sites, *Adv. Funct. Mater.*, 2022, 2204137.

26 J. Zhang, C. Zhang, J. Sha, H. Fei, Y. Li and J. M. Tour, Efficient Water-Splitting Electrodes Based on Laser-Induced Graphene, *ACS Appl. Mater. Interfaces*, 2017, **9**, 26840–26847.

27 J. Zhang, M. Ren, L. Wang, Y. Li, B. I. Yakobson and J. M. Tour, Oxidized Laser-Induced Graphene for Efficient Oxygen Electrocatalysis, *Adv. Mater.*, 2018, **30**(21), 1707319.

28 D. B. Schüpfer, F. Badaczewski, J. Peilstöcker, J. M. Guerra-Castro, H. Shim, S. Firoozabadi, A. Beyer, K. Volz, V. Presser, C. Heiliger, B. Smarsly and P. J. Klar, Monitoring the thermally induced transition from sp3-hybridized into sp2-hybridized carbons, *Carbon N Y*, 2021, **172**, 214–227.

29 M. Pawlyta, J.-N. Rouzaud and S. Duber, Raman microspectroscopy characterization of carbon blacks: Spectral analysis and structural information, *Carbon N Y*, 2015, **84**, 479–490.

30 R. D. Hunter, J. Ramírezramírez-Rico and Z. Schnepp, Iron-catalyzed graphitization for the synthesis of nanostructured graphitic carbons, *J. Mater. Chem. A*, 2022, **10**, 4489–4516.

31 O. Paris, C. Zollfrank and G. A. Zickler, Decomposition and carbonisation of wood biopolymers—a microstructural study of softwood pyrolysis, *Carbon N Y*, 2005, **43**, 53–66.

32 G. Sun, B. Dong, M. Cao, B. Wei and C. Hu, Hierarchical dendrite-like magnetic materials of Fe3O 4, γ-Fe2O3, and Fe with high performance of microwave absorption, *Chem. Mater.*, 2011, **23**, 1587–1593.

33 X. Teng, D. Black, N. J. Watkins, Y. Gao and H. Yang, Platinum-maghemite core-shell nanoparticles using a sequential synthesis, *Nano Lett.*, 2003, **3**, 261–264.

34 E. Bykova, L. Dubrovinsky, N. Dubrovinskaia, M. Bykov, C. McCammon, S. V. Ovsyannikov, H.-P. Liermann, I. Kupenko, A. I. Chumakov, R. Rüffer, M. Hanfland and V. Prakapenka, Structural complexity of simple Fe2O3 at high pressures and temperatures, *Nat. Commun.*, 2016, **7**, 10661.

35 T. Murakami, T. Takahashi, S. Fuji, D. Maruoka and E. Kasai, Development of Manufacturing Principle of Porous Iron by Carbothermic Reduction of Composite of Hematite and Biomass Char, *Mater. Trans.*, 2017, **58**, 1742–1748.

36 B. V L'vov, Mechanism of carbothermal reduction of iron, cobalt, nickel and copper oxides, *Thermochim. Acta*, 2000, **360**, 109–120.

37 H. Wang, C. O. Ogolla, G. Panchal, M. Hepp, S. Delacroix, D. Cruz, D. Kojda, A. Knop-Gericke, K. Habicht, B. Butz and V. Strauss, Flexible CO_2 sensor architecture with selective nitrogen functionalities by one-step laser-induced conversion of versatile organic ink, *Adv. Funct. Mater.*, 2022, 2207406.

38 M. Koebel and E. O. Strutz, Thermal and hydrolytic decomposition of urea for automotive selective catalytic reduction systems: Thermochemical and practical aspects, *Ind. Eng. Chem. Res.*, 2003, **42**, 2093–2100.

39 V. Strauss, H. Wang, S. Delacroix, M. Ledendecker and P. Wessig, Carbon nanodots revised: The thermal citric acid/urea reaction, *Chem. Sci.*, 2020, **11**, 8256–8266.

40 J. Morales and J. L. Tirado, Changes in Crystallite Size and Microstrains from the Thermal Decomposition of Synthetic of Hematite Akaganeite, *J. Solid State Chem.*, 1984, **312**, 303–312.

41 D. G. Chambaere and E. De Grave, The βFeOOH to αFe2O3 phase transformation: structural and magnetic phenomena, *Phys. Chem. Miner.*, 1985, **12**, 176–184.

42 S. Musić, S. Krehula and S. Popović, Thermal decomposition of β-FeOOH, *Mater. Lett.*, 2004, **58**, 444–448.

43 Y. Yang, F. He, Y. Shen, X. Chen, H. Mei, S. Liu and Y. Zhang, A biomass derived N/C-catalyst for the electrochemical production of hydrogen peroxide, *Chem. Commun.*, 2017, **53**, 9994–9997.

44 L. Li, C. Tang, Y. Zheng, B. Xia, X. Zhou, H. Xu and S. Z. Qiao, Tailoring Selectivity of Electrochemical Hydrogen Peroxide Generation by Tunable Pyrrolic-Nitrogen-Carbon, *Adv. Energy Mater.*, 2020, **10**, 1–10.

45 H. Wang, S. Delacroix, O. Osswald, M. Anderson, T. Heil, E. Lepre, N. Lopez-Salas, R. B. Kaner, B. Smarsly and V. Strauss, Laser-carbonization: Peering into the formation of micro-thermally produced (N-doped)carbons, *Carbon N Y*, 2021, **176**, 500–510.

46 R. Zhou, Y. Zheng, M. Jaroniec and S. Z. Qiao, Determination of the Electron Transfer Number for the Oxygen Reduction Reaction: From Theory to Experiment, *ACS Catal.*, 2016, **6**, 4720–4728.

